Appl. Math. Mech. -Engl. Ed., **37**(Suppl.), S31–S42 (2016)

Applied Mathematics and Mechanics (English Edition)

Investigation of horizontal-axis wind turbine (HAWT) blade three-dimensional rotational effect based on field experiments*

Deshun LI[1,2,3], Rennian LI[1,2,3,†], Yinran LI[1,2,3], Xiuyong WANG[1,2,3], Liejiang WEI[1,2,3], Yan QIANG[1,2,3], Zhiqiang LIU[1,2,3]

1. School of Energy and Power Engineering, Lanzhou University of Technology, Lanzhou 730050, China;
2. Gansu Provincial Technology Centre for Wind Turbines, Lanzhou 730050, China;
3. Key Laboratory of Fluid Machinery and Systems, Lanzhou 730050, China

Abstract Field experiments are performed on a two-bladed 33 kW horizontal-axis wind turbine (HAWT). The pressures are measured with 191 pressure sensors positioned around the surfaces of seven spanwise section airfoils on one of the two blades. Three-dimensional (3D) and two-dimensional (2D) numerical simulations are performed, respectively, on the rotor and the seven airfoils of the blade. The results are compared with the experimental results of the pressure distribution on the seven airfoils and the lift coefficients. The 3D rotational effect on the blade aerodynamic characteristics is then studied with a numerical approach. Finally, some conclusions are drawn as follows. From the tip to the root of the blade, the experimental differential pressure of the blade section airfoil increases at first and then decreases gradually. The calculated 3D result of the pressure distribution on the blade surface is closer to that of the experiment than the 2D result. The 3D rotational effect has a significant impact on the blade surface flow and the aerodynamic load, leading to an increase of the differential pressure on the airfoils and their lift coefficient than that with the 2D one because of the stall delay. The influence of the 3D rotational effect on the wind turbine blade especially takes place on the sections with flow separation.

Key words horizontal-axis wind turbine (HAWT), field experiment, three-dimensional (3D) rotational effect, numerical simulation

Chinese Library Classification TK83
2010 Mathematics Subject Classification 76N15

Nomenclature

D,	drag;	F_{t},	tangential force;
F_{a},	axial force;	I,	incline angle;
F_{n},	aerodynamic force;	L,	lift;

* Received Apr. 20, 2016 / Revised Jul. 6, 2016
Project supported by the National Basic Research Program of China (973 Program) (No. 2014CB046201), the National Natural Science Foundation of China (Nos. 51166009 and 51566011), the National High Technology Research and Development Program of China (No. 2012AA052900), and the Natural Science Foundation of Gansu Province (Nos. 1308RJZA283 and 145RJZA059)
† Corresponding author, E-mail: lirn@lut.cn

n,	rotor speed;		north;
P_0,	atmospheric pressure;	α,	angle of attack;
T,	air temperature;	β,	pitch angle;
V,	velocity;	γ,	yaw angle;
ϕ,	relative humidity of air;	θ,	setting angle;
ψ,	angle between directions of inflow and	C_{L},	lift coefficient.

1 Introduction

Wind turbines operate in complicated and multivariate environment with their blades rotating in a very complex three-dimensional (3D) flow. However, the aerodynamic design of available wind turbine blades is mainly based on two-dimensional (2D) data. Therefore, for the future blade design, it is indispensable to study the 3D rotational effect on wind turbine blade. It can be seen from the blind comparison of the American National Renewable Energy Laboratory (NREL) VI experiments that the methods used for prediction of aerodynamic performance of the rotor are not accurate[1]. The wind tunnel experiments are incapable of obtaining accurate work characteristics of the wind turbine operating in actual wind field due to absence of the complicated inflow and influence of the size effect of wind turbine. Thus, a great deal of research on field experiment of wind turbine is necessary to reveal the flow mechanism.

Field experiment on rotor aerodynamics was performed by ECN, NREL, DUT, IC/RAL, and Risø. The final report and database were obtained[2–3]. Barthelmie et al.[4] measured free-stream and wake wind speed profiles of an offshore wind turbine using a ship-mounted Sodar. The program of "the DAN-AERO MW experiments" measured pressure distribution, parameters of inflow, and parameters of wake characteristics and aerodynamic acoustics systematically. The 3D effects, wake characteristics, dynamic stall characteristics, performance evaluation of the wind turbine, and boundary-layer flow over the blade were studied[5]. However, no detailed experimental result, especially the result of wake characteristics, has been published.

Five different models intended to correct for stall delay were tested in a lifting line, prescribed wake vortex scheme. Comparisons were performed with very reliable wind tunnel data measured by the NREL. The models were shown to exhibit inaccuracies in their modelling of the stall delay phenomenon. An overprediction of the loads was generally obtained[6]. The MEXICO and UAE Phase VI and experiments were complementary in many crucial respects, and thus offered unprecedented synergies to better understand and predict rotational augmentation of blade aerodynamics[7]. The stall delay depends slightly on the reduced pressure effect and mainly on the accelerated boundary-layer flow effect. The pressure distribution was controlled by the rotation parameter. The boundary-layer flow was influenced by the radius to local chord ratio. The two contributions to separation delay were discussed[8]. The Reynolds average numerical simulation (RANS) was shown to be suitable for the study of rotational effects. The results showed that the existence of rotational effects was closely related to the presence of radial flows on the boundary layer. The radial flows are mainly caused by the centrifugal force acting on the separated volume of air. The interaction between the centrifugal and Coriolis forces leads to the enhancement of the lift force observed in rotating blades[9]. The 3D rotational effect of wind turbine was studied by Wu and Wang[10–11]. The calculation method was modified to include the 3D rotational effects. The calculated results with and without 3D effects were compared with the experimental data, showing that the calculation was improved by the inclusion of the 3D rotational effects[10–11].

In this study, the field experiments are performed by LUT on a two-bladed 33 kW horizontal-axis wind turbine (HAWT)[12–14]. The 3D and 2D calculation results are compared with the field experimental data of pressure distribution on the blade. The 3D calculation results of lift coefficient are also compared with the 2D data. Then, the studies are performed on the 3D rotational effect on wind turbine blade.

2 Description of experimental facility

2.1 Test wind turbine

The experimental object is a two-bladed 33 kW wind turbine. Its main configurational parameters are as follows: the rotor diameter is 14.8 m, the initial setting angle of blade root is 64.574°, the hub height is 16.12 m, the rated power output is 33 kW, the rated wind speed is 11.0 m/s, the rated speed of rotor is 85 r/min, the cut-in wind speed is 4.0 m/s, and the cut-off wind speed is 23.0 m/s. The blade sections consist of the NACA series airfoils. The experimental wind turbine is installed in county Jingtai, Gansu province, China. Figure 1 shows the field experimental wind turbine.

2.2 Inflow measurement

Three anemometers and a wind direction vane are installed on a meteorology mast at three altitudinal positions (the height of rotor top, the rotor center, and the rotor bottom), respectively, to measure the wind speed and the wind direction, including an anti-icing digital Sonic wind meter at the height of rotor center, offering major reference value of the wind speed and direction. An atmospheric pressure sensor and a temperature and humidity sensor are also installed on the meteorology mast to measure the local atmospheric pressure, air temperature, and humidity. Figure 2 shows the meteorology mast.

Fig. 1 Wind turbine

Fig. 2 Anemometer tower

2.3 Blade surface pressure measurement

The pressure on the blade is measured with 191 tape pressure sensors positioned around the surfaces of seven spanwise section airfoils on one of the two blades. Every pressure sensor is able to gather 3 500 pressure data in a sampling period of 7 s. These analog signals are converted into digital ones by the A/D converter. Then, through the RS485 interface, the digital signals are transmitted to signal adapter installed in the hub with flexible cable stuck on the blade surface. Finally, through the Ethernet interface, the signals are transmitted to an industrial computer by a 50-channel slip-ring. Table 1 shows the position and geometric parameters of the seven airfoils. Figure 3 shows the pressure tape and flexible cable.

Table 1 Position and geometric parameters of seven airfoils

Airfoil number	Relative radial position/%	Initial setting angle/(°)	Chord length/mm
#1	96.53	−54.839 7	213.63
#2	89.84	−55.790 8	237.48
#3	79.84	−56.929 9	283.12
#4	64.84	−59.031 6	350.16
#5	49.77	−60.479 1	414.36
#6	34.23	−62.734 5	485.63
#7	19.84	−64.574 0	549.24

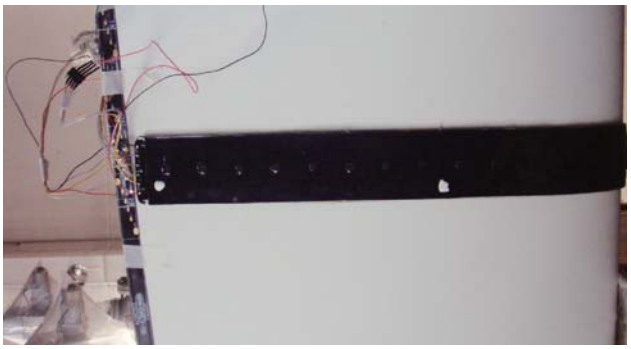

Fig. 3 Pressure tape and flexible cable

2.4 Other measurements from rotor

The active yaw system is based on the worm gear mechanism driven by the DC motor. Taking account of the transmission ratio, the yaw angle is measured by counting the number of turn of the motor shaft. The blade setting angle is controlled by the electro-hydraulic switching valve and measured with the displacement sensor. The botor speed is measured with the electro-optical sensor stuck onto the hub.

3 Experimental conditions

Table 2 shows a set of parameters of an experimental condition, including mainly parameters of inflow and operating condition of the wind turbine.

Table 2 Experimental conditions

Parameter	1	2	3	4	5	6	7	8	9	10	Average value
$V_1/(\mathrm{m{\cdot}s^{-1}})$	12.4	12.2	11.2	10.9	11	11.4	11.4	11.2	11.2	11.8	11.47
$\Psi/(^\circ)$	178	178	177	174	171	170	173	173	175	175	174.4
P_0/Pa	88 210	88 210	88 200	88 200	88 200	88 200	88 180	88 180	88 180	88 180	88 194
$T/^\circ$C	24.4	24.4	24.4	24.4	24.4	24.4	24.4	24.4	24.4	24.4	24.4
$\phi/\%$	59.7	59.7	59.7	59.7	59.7	59.7	59.6	59.6	59.6	59.6	59.66
$n/(\mathrm{r{\cdot}min^{-1}})$	56.34	56.3	56.34	56.3	56.1	56.18	56.1	55.45	54.6	54.69	55.84
$\gamma/(^\circ)$	16.45	16.45	16.45	16.45	16.45	16.45	16.45	16.45	16.45	16.45	16.45
$\beta/(^\circ)$	47.98	47.90	47.98	48.00	48.00	48.05	48.10	47.98	48.00	48.05	48.00

4 Numerical methods for 3D flow of rotor

The governing equations are 3D incompressible Reynolds time-averaged Navier-Stokes equations and continuity equation. The turbulence mode is the standard k-ε mode. The computation domain of the wind turbine is discretized with the structured mesh. The mesh is comprised of 25 304 723 cells. The moving reference frame (MRF) is used to incorporate the rotor rotation. The standard wall functions are used to compute the near wall flow. Second-order discretization schemes are used for the variables and the SIMPLE algorithm to solve the pressure-velocity coupling. The velocity inflow boundary condition is implemented at the inflow boundary with the average inflow velocity value of 11.47 m/s, and the turbulence intensity is assumed to be 10%. The pressure outlet boundary condition is specified at the outflow boundary with the average atmospheric pressure value of 88 194 Pa. No-slip assumption is taken as the boundary condition on the blade surface.

The parameters of simulation are consistent with the average value in Table 2. The density of inflow is 0.962 kg/m^3, which is calculated by the following formula:

$$\rho' = \rho_0 \frac{273}{273+T} \frac{p - 0.0378\phi p_\mathrm{b}}{0.1013},$$

where ρ' represents the density of wet air (kg/m^3), ρ_0 represents the density of dry air under the condition of temperature of 0 °C and atmospheric pressure of 101.325 kPa (kg/m^3), p represents the full pressure of wet air (MPa), and p_b represents the partial pressure of steam in saturated air at the temperature of T (MPa).

5 Numerical methods for 2D flow of airfoil

The governing equations are 2D incompressible Reynolds time-averaged Navier-Stokes equations and continuity equation. The turbulence mode is the standard k-ε mode. The standard wall functions are used to compute the near wall flow. Second-order discretization schemes are used for the variables and the SIMPLE algorithm to solve the pressure-velocity coupling. The velocity inflow boundary condition is implemented at the inflow boundary with the turbulence intensity assumed to be 10%. The pressure outlet boundary condition is specified the outflow boundary with the average atmospheric pressure value of 88 194 Pa. No-slip assumption is taken as the boundary condition on the blade surface.

The density of inflow is consistent with 3D simulation. Table 3 shows the angle of attack and inflow velocity of the seven airfoils under the experimental condition, which is calculated by the blade element theory. Figure 4 is the velocity and force diagram of airfoil.

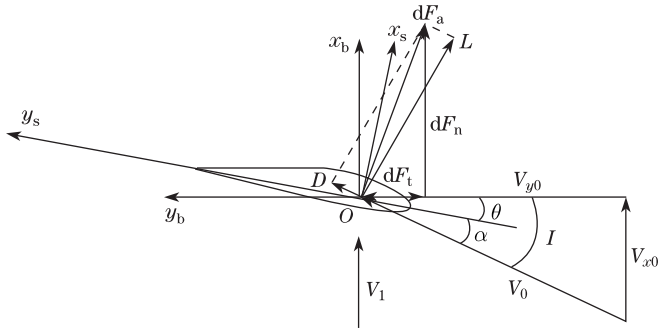

Fig. 4 Velocity and force diagram of airfoil

Table 3 Angle of attack and inflow velocity of seven airfoils

Airfoil	#1	#2	#3	#4	#5	#6	#7
α/(°)	8.54	8.68	9.47	11.24	15.61	23.07	36.68
V_0/(m·s^{-1})	43.26	40.48	36.36	30.28	24.38	18.72	14.32

6 Results and analysis

6.1 Comparison and analysis of pressure distribution

Figures 5–11 show the static pressure distribution on seven airfoils obtained from the field experiment, 2D calculation, and 3D calculation, respectively, under the above-mentioned experimental conditions.

6.1.1 Analysis of experimental result

From the blade tip to its root, the spanwise differential pressure on the blade section airfoil increases at first and then decreases gradually. From the tip of blade to Airfoil #2, the pressure values increase on the pressure surface and decrease on the suction surface. The differential pressure increases gradually. It is mainly caused by the 3D flow near the blade tip. From Airfoil #2 to the root of blade, the pressure values decrease on the pressure surface and increase on the suction surface. The differential pressure decreases gradually.

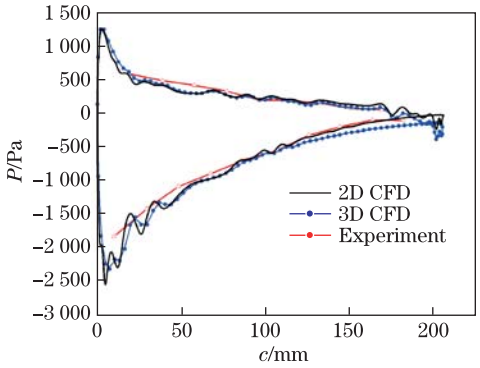

Fig. 5 Static pressure distribution on Airfoil #1

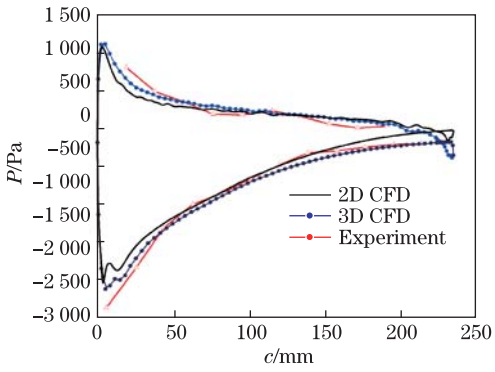

Fig. 6 Static pressure distribution on Airfoil #2

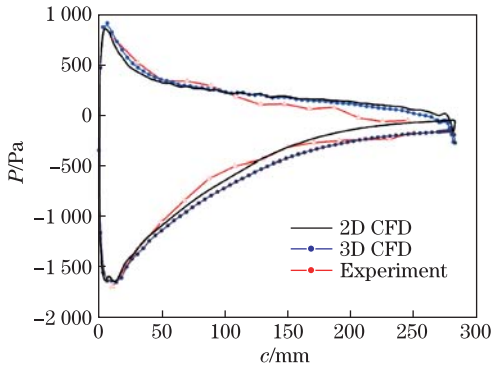

Fig. 7 Static pressure distribution on Airfoil #3

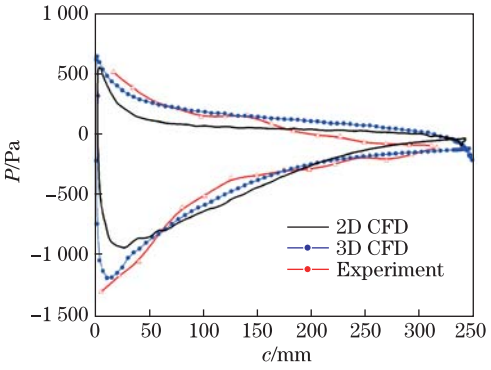

Fig. 8 Static pressure distribution on Airfoil #4

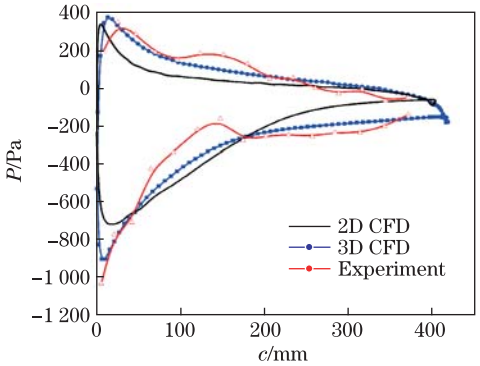

Fig. 9 Static pressure distribution on Airfoil #5

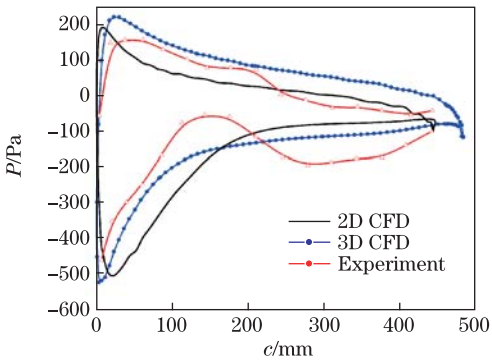

Fig. 10 Static pressure distribution on Airfoil #6

For Airfoil #1 to Airfoil #4, the pressure on the suction surface decreases gradually from the trailing edge to the leading edge. The pressure gradient is ever-increasing as approaching the leading edge. As for Airfoil #5 to Airfoil #7, the pressure on the suction surface from the trailing edge to the leading edge decreases at first, then increases, and then decreases again. Therefore, there is a peak on every pressure distribution curve on the suction surface. The closer the airfoil position is to the blade root, the closer the position of peak is to the leading edge and the bigger the value of the peak is. Therefore, the flow separation and secondary flow occur on the suction surface. The closer the airfoil position is to the blade root, the closer the

initiative flow separation is to the leading edge. Airfoil #7 works at a large angle of attack 36.68°. There is an excessive flow separation from the airfoil. In addition, the effect of 3D flow at the root of blade and around the hub is very big so that the pressure is unsteady. This can be seen in Figs. 12 and 13, where the streamline on suction and pressure surface of the blade is shown.

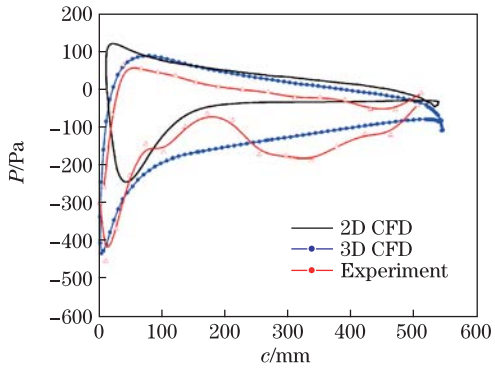

Fig. 11 Static pressure distribution on Airfoil #7

Fig. 12 Limit streamline on suction surface of blade

Fig. 13 Limit streamline on pressure surface of blade

6.1.2 Comparison of results between numerical calculation and experiment

In general, the 3D result is closer to the experimental data than the 2D result. The agreement of pressure curves with those of experiment is better near the leading edge than near the trailing edge. The 3D and 2D results agree well with the experimental data from Airfoil #1 to Airfoil #5. However, there is a larger deviation on Airfoil #6 and Airfoil #7. The main reason is as follows. Airfoils #6 and #7 work at a large angle of attack of 23.07° and 36.68°, respectively. There is excessive flow separation from the airfoils. In this case, the calculation accuracy with the numerical methods used in this paper reduces relatively.

As for the suction surface, the 2D result is generally higher than the 3D and experimental data, especially near the leading and trailing edges. The 3D result is closer to the experimental data than the 2D result. However, on either 3D or 2D curve, there is no such peak as on the experimental curves from Airfoil #5 to Airfoil #7. On the pressure surface, the 2D result is generally lower than the 3D data. The nearer the airfoil is to the blade root, the larger the data deviation is. This phenomenon is identical for both 3D and 2D results.

It can be seen from the above analysis that, with the rotation of blade, the 3D rotational effect has a larger impact on the blade aerodynamic load that will lead to the increase of the differential pressure on the airfoil.

6.2 Comparison of lift coefficient

Table 4 shows the lift coefficients of the seven airfoils obtained with approach of the 3D and 2D calculation, respectively. It can be seen from this table that the lift coefficients of 3D approach are increased by 0.82%, 8.21%, 3.82%, 6.27%, 11.46%, 18.79%, and 82%, respectively, over that of 2D approach from Airfoil #1 to Airfoil #7. In general, the 3D data are greater than the 2D data. The relative deviations are less than 12% from the middle of the blade to the tip, which is the main region for power output. The closer the airfoil is to the blade root, the bigger the deviation is. The lift coefficient of Airfoil #1 of the 3D approach is almost equal to the 2D data at the blade tip. The lift coefficient of Airfoil #7 at the blade root is increased by 82% over the 2D result. The reason is mainly as follows. The finite blade length and the rotation of the blade cause a strong 3D flow. At the blade tip, it leads to pressure increasing on the blade suction surface and decreasing on the pressure surface with a little amount of air flowing from the pressure surface to the suction surface around the blade tip. It can be seen from Fig. 14 that the oblique streamlines take place on the suction surface and the pressure surface at the blade tip. Therefore, the differential pressure of 3D result on the airfoils drops. It results in an almost identical pressure distribution and lift coefficient obtained with both 3D and 2D approaches. Airfoils #6 and #7 are closer to the blade root, and their angles of attack are 23.07° and 36.68°, respectively. The flow around the airfoils is related to the stall flow condition with a large angle of attack. Figures 12 and 13 show that very strong three-dimensional flow and flow separation take place at the blade root. The stall delay occurs on the airfoils closer to the blade root because of a strong three-dimensional rotation effect. It ultimately results in the fact that the lift coefficients of the 3D result are obviously larger than the 2D results. This can be testified by the analysis of flow fields around the seven airfoils as follows.

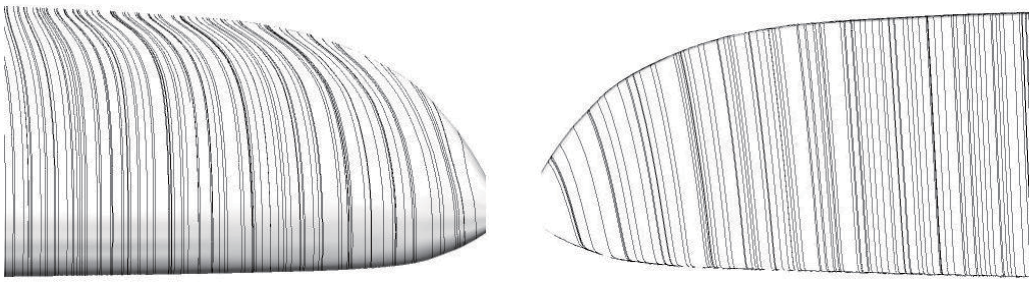

Fig. 14 Limit streamline on suction surface (left) and pressure surface (right) at blade tip

Table 4 Comparison of lift coefficients of seven airfoils

Airfoil number	#1	#2	#3	#4	#5	#6	#7
C_{L} (3D)	1.057 2	1.221 5	1.258 9	1.275 2	1.312 9	1.330 4	1.520 2
C_{L} (2D)	1.048 6	1.128 8	1.212 6	1.120 0	1.177 9	1.200 0	0.835 2

6.3 Comparison of flow fields

Figures 15–21 show the streamlines around the seven airfoils obtained with 3D and 2D simulation, respectively. It can be seen from Figs. 15 and 16 that both the 2D and 3D calculation results show that the flows around Airfoils #1 and #2 are attached flows, and no flow separation occurs on them. From Airfoil #3 to Airfoil #7, flow separation occurs on the airfoils, and the closer to the blade root is, the greater the attack angle of the airfoil is, and the stronger flow separation is thereby. The separation point also moves towards the leading edge gradually.

However, compared with the 2D calculation results, the flow separation points of the 3D calculation are closer to the airfoil trailing edge. Moreover, the flow separation region on the airfoil surface is less than that of the 2D calculation results. This indicates that, due to the rotation of the wind turbine rotor, the flow field around blade is affected by the 3D rotation effect and generates spanwise flow over the blade. This flow leads to the stall delays of airfoil, meanwhile delays the occurrence of separation point, and reduces the flow separation region on the airfoil surface. The stall delay affects the lift characteristics of the airfoil ultimately and makes the differential pressure and lift coefficient of each airfoil to increase (larger than that of the 2D airfoil).

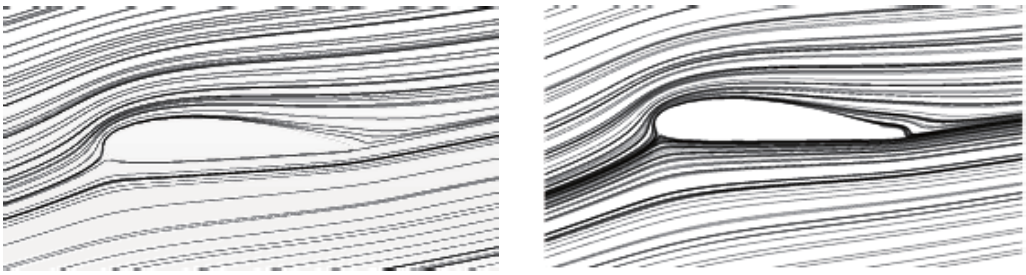

Fig. 15 Streamlines with 2D (left) and 3D (right) simulation of Airfoil #1

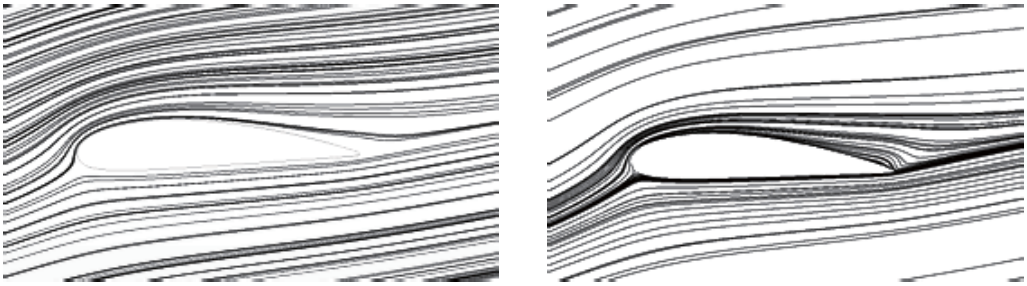

Fig. 16 Streamlines with 2D (left) and 3D (right) simulation of Airfoil #2

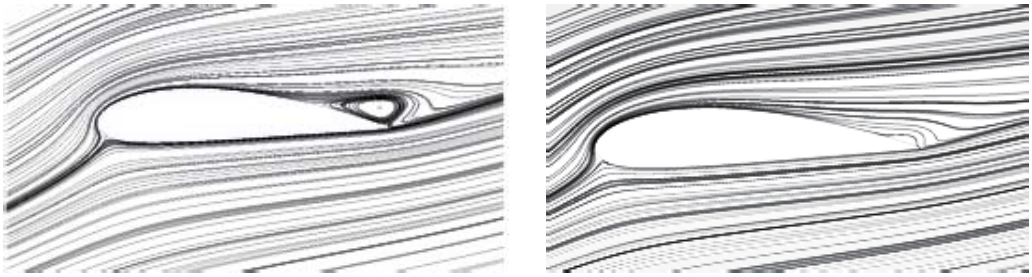

Fig. 17 Streamlines with 2D (left) and 3D (right) simulation of Airfoil #3

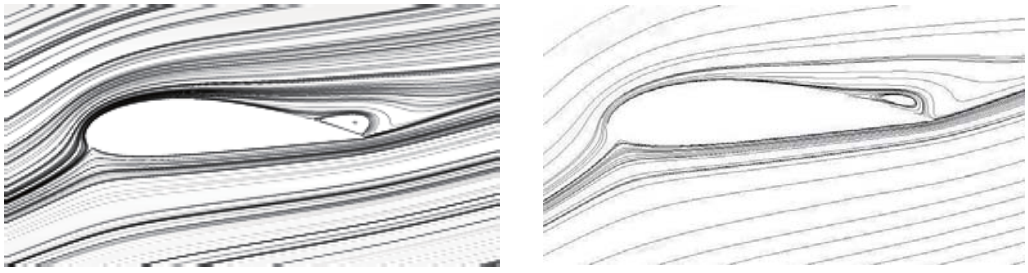

Fig. 18 Streamlines with 2D (left) and 3D (right) simulation of Airfoil #4

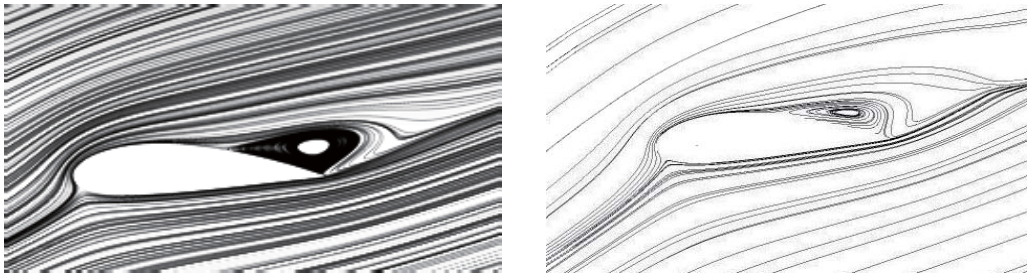

Fig. 19 Streamlines with 2D (left) and 3D (right) simulation of Airfoil #5

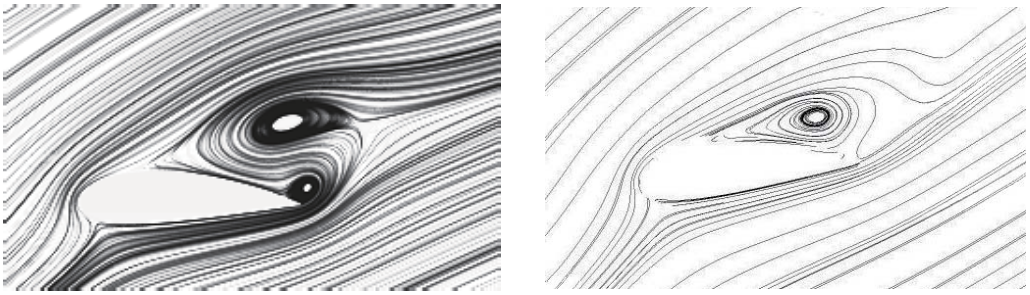

Fig. 20 Streamlines with 2D (left) and 3D (right) simulation of Airfoil #6

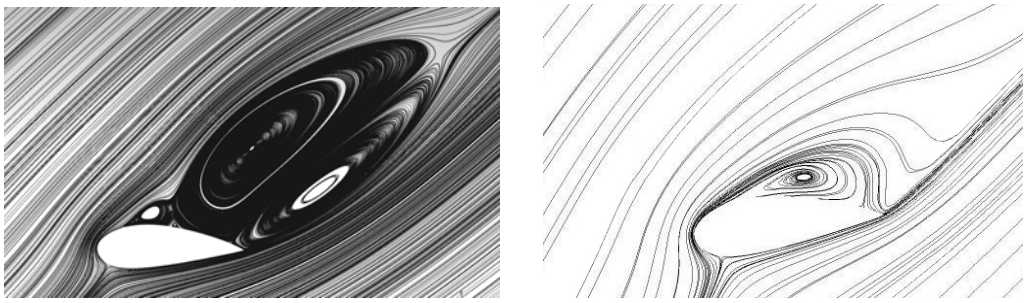

Fig. 21 Streamlines with 2D (left) and 3D (right) simulation of Airfoil #7

Combined with Figs. 5–11, Figs. 15–21, and Table 4, it can be seen clearly that the 3D rotation effect affects the blade aerodynamic characteristics and flow characteristics. It will be the most conspicuous on the sections (such as the sections where Airfoils #5, #6, and #7 are located) where a large angle of attack leads the flow to separate, and causes a larger increase of their lift coefficients. When the flow on the blade surface is attached flow or there is a small range of separated flow near the trailing edge (such as the sections where Airfoils #1, #2, #3, and #4 are located), the 3D rotation effect is not obvious and has less impact on their lift coefficient, the increase of the lift coefficient is less than ten percent of the value of the 2D airfoil. Therefore, if the flow separation does not occur on the surface of the blade or there is only a small separation area near the trailing edge, high accuracy can be achieved by the 2D aerodynamic data of the airfoil for the design and calculation of the aerodynamic performance of the rotor. Otherwise, the 2D data must be corrected by means of the appropriate model of the 3D rotation effect.

7 Conclusions

The influence of the 3D rotational effect on the aerodynamic characteristics of wind turbine blade is studied by means of comparing the pressures and the lift coefficients of the seven blade section airfoils and their flow characteristics. The main conclusions are as follows.

From the tip to the root of the blade, the experimental differential pressure of the blade section airfoil increases at first and then decreases gradually. The pressure distribution on the blade surface obtained with the 3D numerical approach is closer to the experiment results than that with the 2D one.

Compared with the 2D data, the 3D rotational effect has a larger impact on the blade surface flow and aerodynamic load, leading to an increase of the differential pressure on the airfoils and their lift coefficient than that with the 2D one because of stall delay. The closer the airfoil is to the blade root, the more obvious the 3D rotational effect is. The lift coefficient of Airfoil #7 at the blade root increases by 82% over the 2D result.

The influence of the 3D rotation effect on aerodynamic characteristics of wind turbine blade especially takes place on the sections with a large angle of attack and flow separation. When the flow on the blade surface is attached flow or there is a small range of flow separation near the trailing edge, the influence of the 3D rotation effect is not obvious.

References

[1] Simms, D., Schreck, S., Hand, M., and Fingersh, L. J. *NREL Unsteady Aerodynamics Experiment in the NASA-Ames Wind Tunnel: a Comparison of Predictions to Measurements*, National Renewable Energy Laboratory, Colorado (2001)

[2] Schepers, J. G., Brand, A. J., Bruining, A., Graham, J. M. R., Hand, M. M., Infield, D. G., Madsen, H. A., Paynter, R. J. H., and Simms, D. A. *Final Report of IEA Annex* XIV: *Field Rotor Aerodynamics*, ECN-C-97-027 (1997)

[3] Schepers, J. G., Brand, A. J., Bruining, A., Graham, J. M. R., Hand, M. M., Infield, D. G., Madsen, H. A., Paynter, R. J. H., and Simms, D. A. *Final Report of IEA Annex* XVIII: *Enhanced Field Rotor Aerodynamics Database*, ECN-C-02-016 (2002)

[4] Barthelmie, R. J., Folkerts, L., Larsen, G. C., Rados, K., Pryor, S. C., Frandsen, S. T., Lange, B., and Schepers, G. Comparison of wake model simulations with offshore wind turbine wake profiles measured by Sodar. *Journal of Atmospheric and Oceanic Technology*, **23**, 888–901 (2006)

[5] Aagaard-Madsen, H., Bak, C., Schmidt-Paulsen, U., Gaunaa, M., Fuglsang, P., Romblad, J., Olesen, N. A., Enevoldsen, P., Laursen, J., and Jensen, L. *The DAN-AERO MW Experiments: Final Report*, Risø-R-1726 (EN) (2010)

[6] Breton, S. P., Coton, F. N., and Moe, G. A study on rotational effects and different stall delay models using a prescribed wake vortex scheme and NREL phase VI experiment data. *Wind Energy*, **11**, 459–482 (2008)

[7] Schreck, S., Sant, T., and Micallef, D. *Rotational Augmentation Disparities in the MEXICO and UAE Phase* VI *Experiments*, NREL, CP-500-47759 (2010)

[8] Dumitrescu, H. and Cardos, V. Rotational effects on the boundary-layer flow in wind turbines. *AIAA Journal*, **8**, e69612 (2013)

[9] Herraez, I., Stoevesandt, B., and Peinke, J. Numerical study of rotational effects on wind turbines. 12*th German Wind Energy Conference*, Bremen (2015)

[10] Wu, Y. and Wang, T. G. Prediction of the unsteady aerodynamic characteristics of wind turbine blades with 3D rotational effects (in Chinese). *Chinese Journal of Computational Mechanics*, **25**(1), 100–103 (2008)

[11] Wu, Y. and Wang, T. G. Prediction of three-dimensional rotational effect on blade aerodynamic characteristics (in Chinese). *Acat Aerodynamica Sinica*, **24**(2), 200–203 (2006)

[12] Li, R. N., Yuan, S. K. Wei, L. J., Li, D. S., and Li, Y. R. Measurement and calculation of blade surface pressure for a wind turbine in field (in Chinese). *Journal of Experiments in Fluid Mechanics*, **26**, 52–56 (2012)

[13] Li, D. S. and Li, R. N. Field experiment of blade surface pressure of an HAWT. *Applied Mechanics and Materials*, **291-294**, 445–449 (2013)

[14] Li, D. S., Li, R. N., Wang, X. Y., Wei, L. J., Li, Y. R., Qiang, Y., and Liu, Z. Q. Investigation of three-dimensional effect on blades of a wind turbine based on field experiments (in Chinese). *Applied Mathematics and Mechanics*, **34**, 1073–1082 (2013)